CHAPTER 4

RESULTS AND DISCUSSIONS

As the experimental designed in previous chapter, the electrical properties of a-C:Mo will be discussed. The properties of a-C:Mo films would be studied, but still not applied for application in this experiment due to their cathodic arc deposition is still a high cost technique and provide very thin film. The properties of ZnO, ZnO:Al, nitride and carbide of stainless steel would be investigated for bipolar plates application. So the results of interfacial contact resistance, corrosion resistance or even static water contact angle are needed to know.

4.1 Properties of a-C:Mo films

The Mo-DLC films were deposited in vacuum chamber. Film sheet resistance was measured in-situ during deposition process. After deposition, the samples were annealed in ambient air up to 515 K.

4.1.1 Films resistance

Film resistance was measured during film thickness increasing. Assumed that film deposition rate was constant during film deposition. Figure 4.1 show film resistance and resistivity changing during deposition at Mo/C pulse was 0.05. The maximum sheet resistance for no bias was detected at 4.52×10^{8} Ω and reduced to 3.03×10^{4} Ω at the end of deposition. For carbon selective bias at -100 volt, the maximum resistance was 5.26×10^{8} Ω and 6.07×10^{7} Ω in minimum.

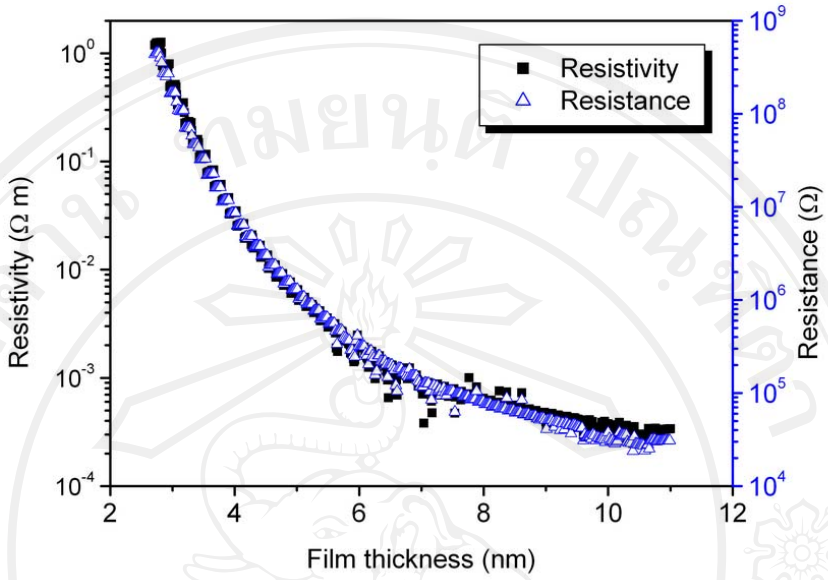

(a)

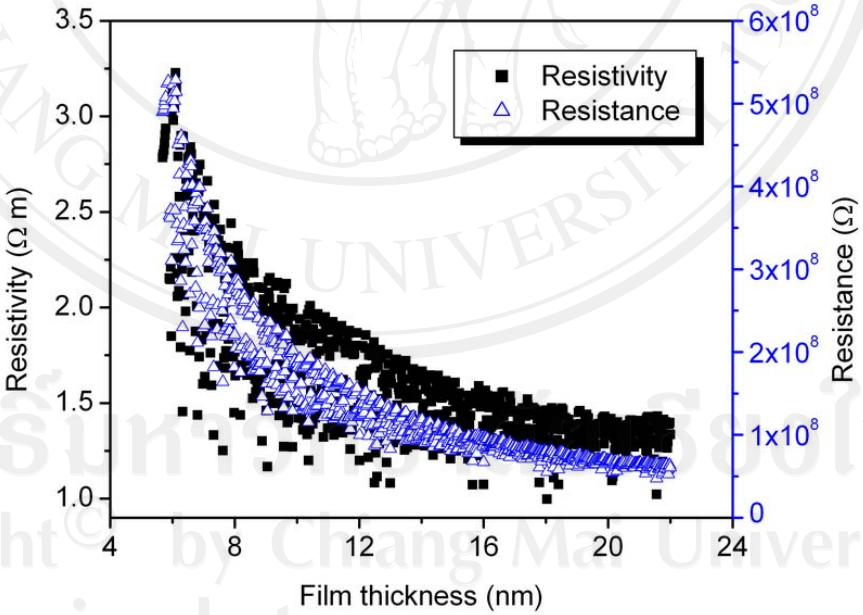

(b)

Figure 4.1 Film resistance during deposition process of Mo/C pulse was 0.05, with no bias (a) and carbon selective bias at -100 volt (b).

Film resistance was changing in the same characteristic for other Mo/C ratio and other bias voltage (see appendix A-2). Table 4.1 and Figure 4.2 show the resistance after deposition at different Mo/C ratio with no substrate bias. Film thickness was in the range 8 to 13 nm. The resistivity was 0.035 Ω cm maximum and 2.27×10^{-4} Ω cm minimum.

Table 4.1 Condition and results of film deposition at different Mo:C pulse ratio with no bias.

Mo:C pulse	Sample number	Sheet resistance (Ω)	Film thickness (nm)	Resistivity (Ω cm)
0:1	Exp 018	> 500 M	8	> 400
1:20	Exp 012	32.24×10^{3}	11	3.55×10^{-2}
1:15	Exp 011	8.44×10^{3}	11	9.28×10^{-3}
1:10	Exp 013	2723	13	3.54×10^{-3}
1:5	Exp 014	622.0	11	6.84×10^{-4}
3:10	Exp 015	230.0	12	2.76×10^{-4}
2:5	Exp 017	206.0	11	2.27×10^{-4}

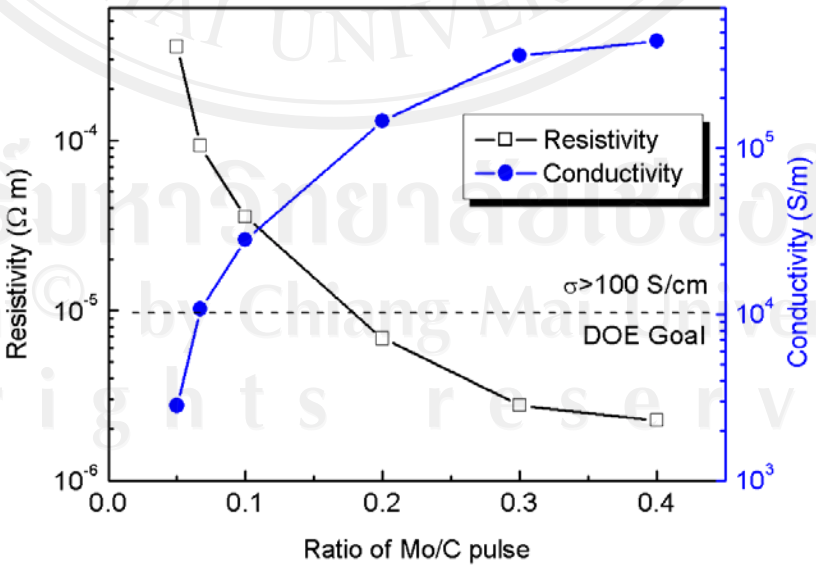

Figure 4.2 Film resistivity and conductivity after deposition at different Mo:C pulse ratio with no bias.

Table 4.2 and Figure 4.3 shown the resistance and resistivity after deposition in case of carbon selective bias. The pulse negative bias was applied from -100 to -1,000 volt at constant Mo/C pulse ratio of 0.05. Film thickness varies between 21 and 28 nm. Film resistivity was 276.64 Ω cm maximum at -200 volt bias and minimum 3.63 Ω cm at -1,000 volt bias.

Table 4.2 Conditions and results of film deposition at Mo:C = 1:20 pulse with different bias voltage.

Bias (V)	Sample number	Sheet resistance (MΩ)	Film thickness (nm)	Resistivity (Ω cm)
-100	Exp 037	75.8	22	166.76
-200	Exp 038	98.8	28	276.64
-400	Exp 039	50.1	25	125.25
-600	Exp 040	16.55	21	34.755
-800	Exp 041	1.548	21	3.2508
-1,000	Exp 042	1.511	24	3.6264

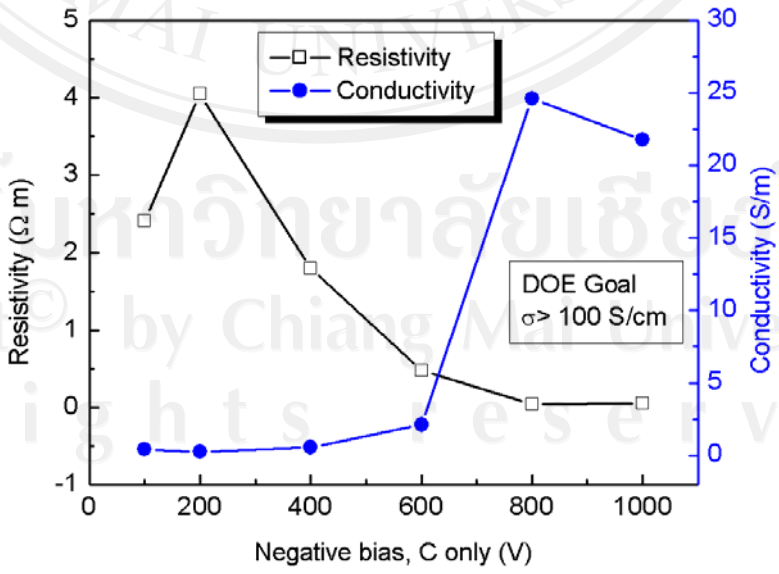

Figure 4.3 Film resistivity and conductivity after deposition at Mo:C = 1:20 pulse with different bias voltage.

4.1.2 Film activation energy

Although the exact conduction mechanism of metal-containing amorphous carbon films remains unclear, it is generally believed that the introduced metal into the amorphous carbon films will increase the complexity of the electronic transport properties which is mainly controlled by sp^2 clusters. Huang et al. (2000) have reported that there are two types of conduction mechanisms in molybdenum-containing diamond-like carbon films; thermal activation and tunneling coexist, and they dominate the conduction behavior in the high and low temperature regimes, respectively. They found that a conductivity turning point exist around 115 K. Above the turning point, the electrical conductivity, σ, of the film can be written as an exponential function of temperature, T, in the form

$$\sigma(T) = \sigma_0 \exp(-E_A/k_B T) \quad , \qquad (4.1)$$

where E_A is the activation energy for electric conduction, σ_0 is the pre-exponential factor is determined by the charge carrier mobility and density of states, and k_B is the Boltzmann constant. Since we operated above room temperature in our tests, the application of this equation is well justified.

Figure 4.4 shows an Arrhenius plot of the reciprocal temperature and ln(σ) obtained from the temperature dependent sheet resistance measurement. In our temperature test range, the film conductivity approximately followed equation (4.1), i.e., a linear relationship between ln(σ) and the reciprocal of temperature. A linear fit of ln(σ) versus $1/T$ was taken to determine the approximate activation energy and the pre-exponential factor for the temperature range 300-515 K. The results are shown in Figure 4.5. The calculated σ_0 values for the film prepared for a pulse ratio of 0.05< Mo/C < 0.4 without bias were in the range of 10^4-10^5 Ω^{-1} m^{-1}, and less than 10^4 Ω^{-1} m^{-1} for various substrate bias at 0.05 Mo/C pulse ratio.

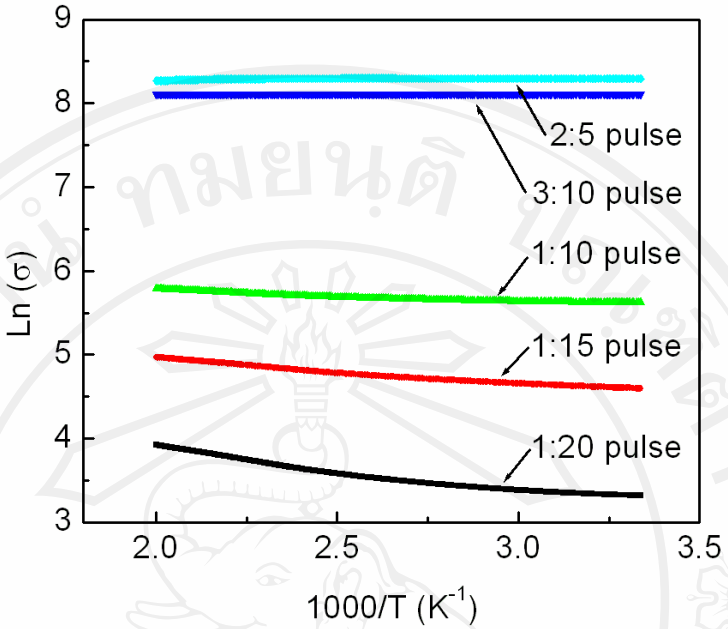

(a)

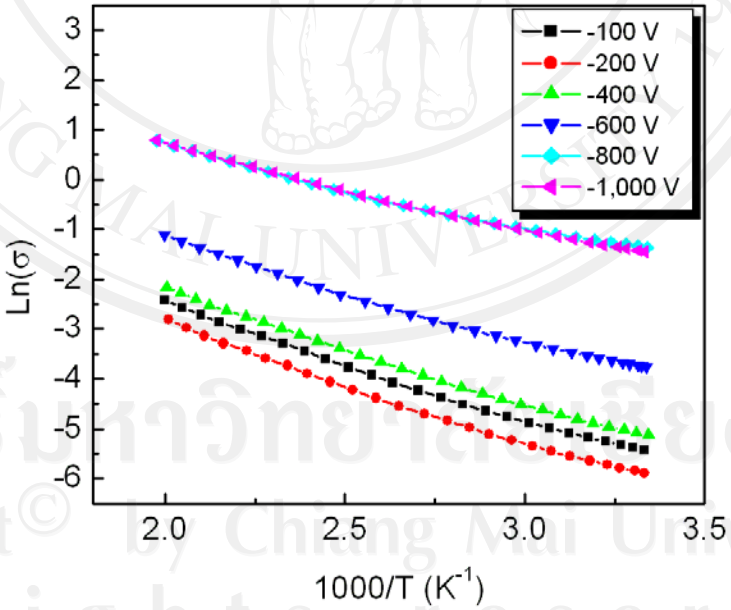

(b)

Figure 4.4 Arrhenius plot of the film conductivity at (a) varies Mo/C deposition pulse ratio without bias and (b) under different substrate bias voltage at constant Mo/C deposition pulse ratio of 0.05.

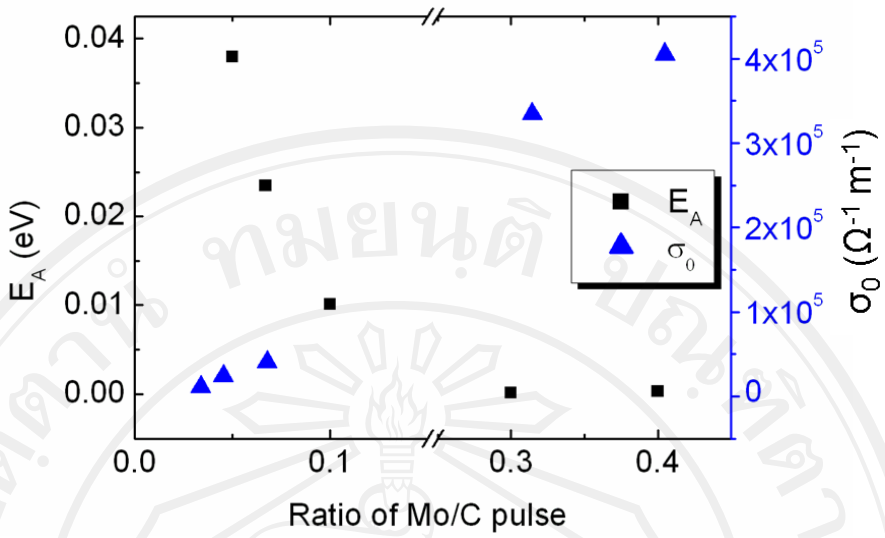

(a)

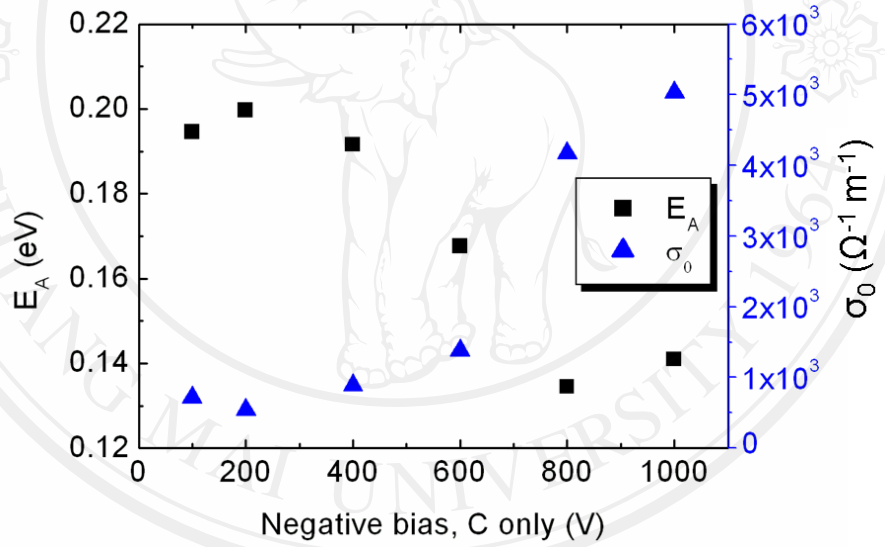

(b)

Figure 4.5 Electrical activation energy and pre-exponential factor of a-C:Mo film deposited at (a) different Mo/C deposition pulse ratios without bias and (b) different carbon selective bias voltage at constant Mo/C deposition pulse ratio of 0.05.

The activation energy and pre-exponential factor show varies in opposite direction when Mo:C ratio pulse increased and also for increasing substrate bias voltage. In our Mo-DLC film, the calculated σ_0 value for the film prepared for 0.05<Mo/C<0.4 pulse ratio with no bias were in the range of 10^2-10^3 $\Omega^{-1}.cm^{-1}$, and less than 10^2 $\Omega^{-1}.cm^{-1}$ for varies substrate bias at 0.05 Mo/C pulse ratio.

4.1.3 Film microstructure

Visible Raman spectroscopy would allow us to approximately deduce the sp^2/sp^3 ratio. The Raman spectroscopy was done with the 514 nm line of an argon ion laser over the range of 900-2000 cm^{-1}. The result was shown in Figure 4.6.

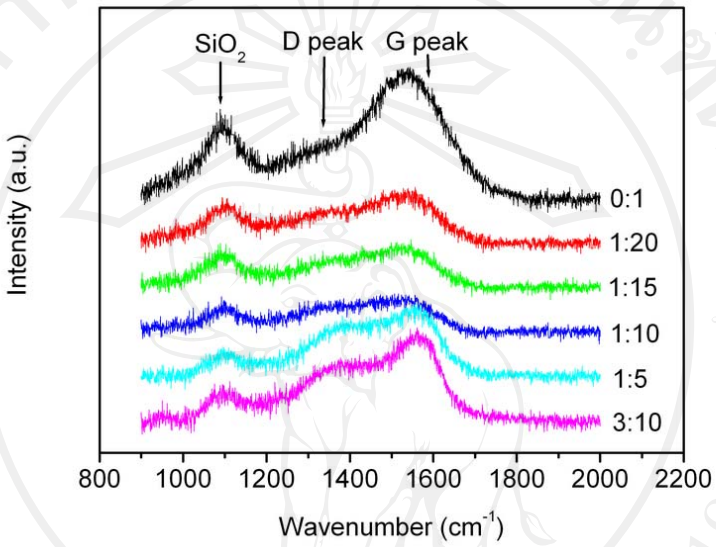

(a)

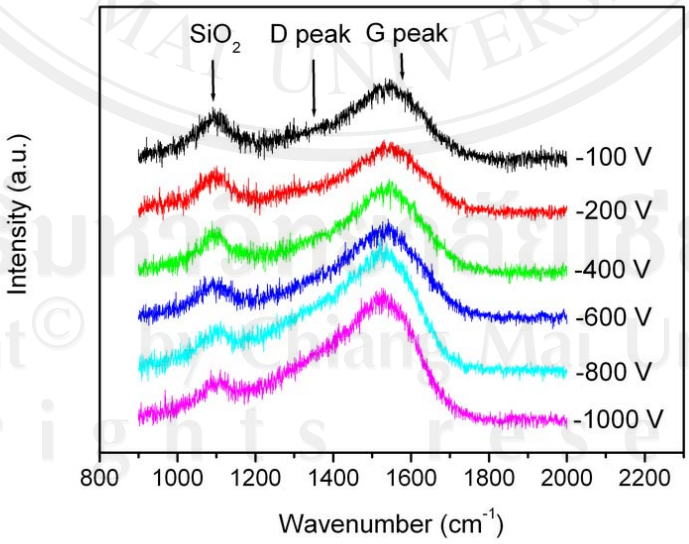

(b)

Figure 4.6 Raman spectra of the film prepared at (a) various Mo/C pulse ratio and (b) various bias voltage at constant Mo/C deposition ratio of 0.05.

The Raman spectra were fitted by Gaussian distributions for the disorder ('D') and graphite ('G') peaks. The peak intensity ratio (I_D/I_G), plotted as a function of Mo/C and bias voltage, are given in Figure 4.7.

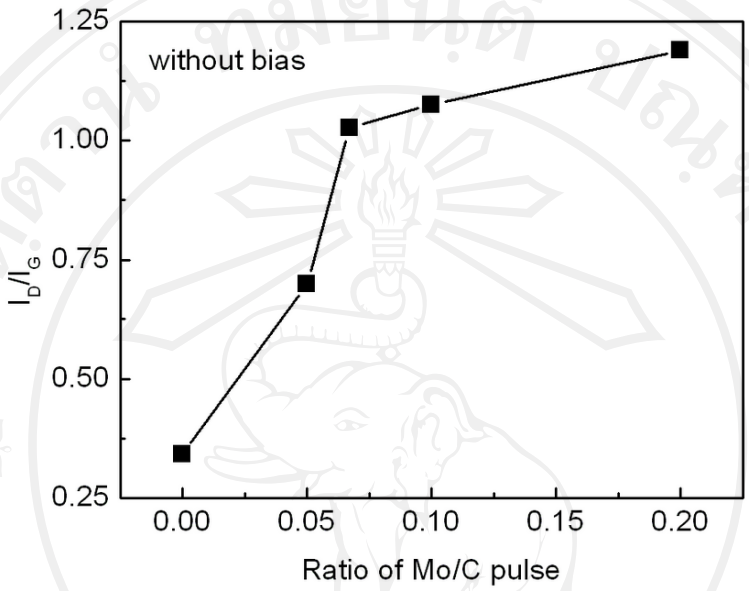

(a)

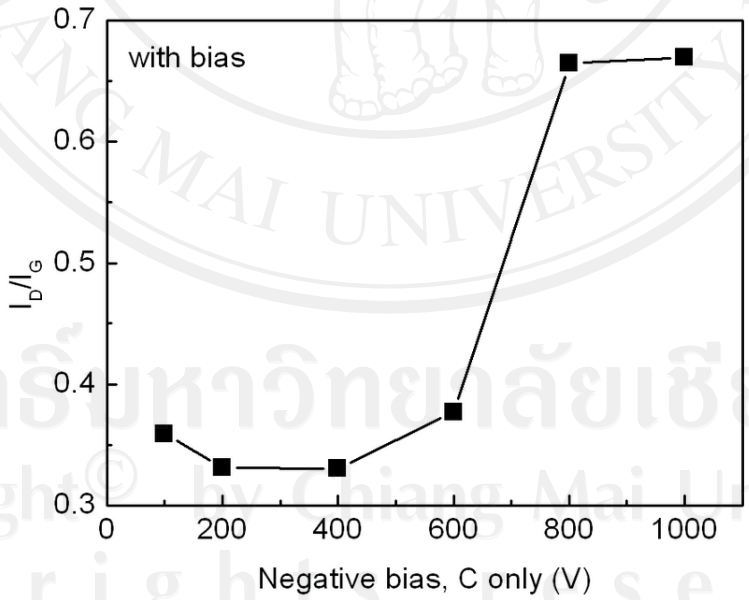

(b)

Figure 4.7 Variation of the Raman intensity ratio, D and G peaks, as a function of (a) various Mo/C deposition pulse ratios without bias and (b) various carbon selective bias voltages at constant Mo/C deposition ratio of 0.05.

It can be seen that the I_D/I_G ratio increases with increasing Mo/C ratio (Figure 4.7a). Looking at the influence of substrate bias on the intensity ratio of I_D/I_G, one can see that I_D/I_G decreases slightly from an initial value of 0.36, reaches a minimum at approximately between 300-400 V bias voltage, and then increases rapidly (Figure 4.7b). We quote applied bias voltage, however, one should note that the actual potential on the glass slide surface is not exactly the applied bias voltage, which is applied to the holder, rather, a time-dependent voltage drop appears between holder and substrate surface. Since the actual surface potential is not well known, we quote the applied voltage. The I_D/I_G ratio is an indication of sp^2 to sp^3 bonds in the deposited films (Ferrari and Robertson, 2000). It can be observed that the I_D/I_G ratio has a trend that correlates with the pre-exponential factor σ_0 shown in Figure 4.5. This can be explained by an increase in the conductive pathways caused by an increase in the fraction of conductive graphite-like material. However, the varying trends of I_D/I_G ratio of a-C:Mo films with substrate bias are the same as that of the pure ta-C and ta-C:W films (Tay et al., 1998).

4.2 Properties of ZnO:Al, ZnO, Nitride and Carbide

ZnO:Al and ZnO films were prepared by reactive magnetron sputtering. Experiment conditions and results shown in Table 4.3 and Table 4.4 respectively. Table 4.5 to Table 4.8 were shown the sample number and condition of gas plasma immersion.

Table 4.3. Experimental conditions and results of ZnO:Al thin film.

Experiment	O_2 flow (sccm)	Ar flow (sccm)	Thickness (nm)	Resistivity (Ω-cm)
Exp 109	5	40	4,343	3.50×10^{-2}
Exp 110	10	40	557	9.47×10^{-3}
Exp 111	20	40	396	8.21×10^{-2}
Exp 112	2	40	3,873	5.42×10^{-4}

Table 4.4. Experimental conditions and results of ZnO thin film.

Experiment	O_2 flow (sccm)	Ar flow (sccm)	Thickness (nm)	Resistvity (Ω-cm)
Exp 113	2	40	4,785	$6.22x10^{-4}$
Exp 114	5	40	7,766	$1.40x10^{-3}$
Exp 115	10	40	4,261	$7.07x10^{-3}$
Exp 116	20	40	492	$1.50x10^{-3}$

Table 4.5. Experimental conditions of N_2+C_2H_2 plasma immersion.

Experiments	N_2 flow (sccm)	C_2H_2 flow (sccm)
Exp 118	50	10
Exp 119	50	15
Exp 120	50	5

In the beginning, we prepared nitridation with pure N_2 at lower pressure about 60 mtorr, but we saw no film. We also try carburization by using C_2H_4 gas plasma treatment, there are some black film on the top surface of AISI specimen. But the film began creaking after 7 minute of deposition. For some immersion condition, we got a black, hard and highly insulator.

Table 4.6 Experimental conditions of AISI 304 plasma nitriding by "Pinnacle plus" power supply.

Experiments	N_2+H_2 flow (sccm)	Pressure (torr)	Time (min)
Exp 127	60	1.0	60
Exp 128	60	1.0	30
Exp 129	70	2.5	60
Exp 130	70	2.5	30
Exp 131	80	3.5	60
Exp 132	80	3.5	30

Table 4.7 Experimental conditions of AISI304 plasma nitriding by Cober power supply.

Experiments	N_2+H_2 flow (sccm)	Pressure (torr)	Time (min)
Exp 133	60	1.0	60
Exp 134	60	1.0	30
Exp 135	70	2.5	60
Exp 136	70	2.5	30
Exp 137	80	3.5	Fail
Exp 138	70	2.5	45

Table 4.8 Experimental conditions of N_2 and CH_4 gases plasma immersion.

Experiments	N_2 flow (sccm)	CH_4 flow (sccm)
Exp 162	60	10
Exp 163	50	20
Exp 164	40	30
Exp 165	70	0

Note :

The specimen holder should be cleaned by polishing, cleaned by ethanol and dry every time for next experiment. The insulating film coated on the holder surface will reduced bias current (and also plasma current) and hence reduce the specimen heating.

4.2.1 Interfacial contact resistance (ICR)

The interfacial contact resistance (ICR) of carbon paper and copper plate was investigated first. The available ICR of treated AISI 304 specimens were shown as follow.

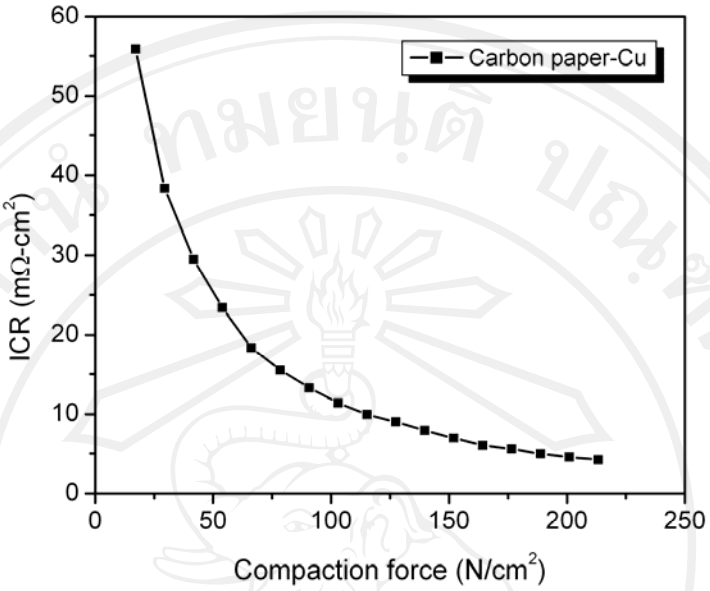

Figure 4.8 Interfacial contact resistance (ICR) of carbon paper and copper plate.

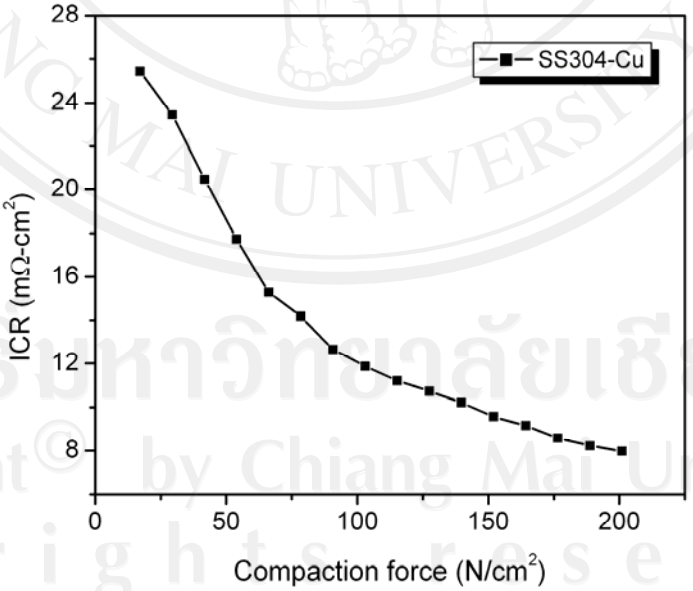

Figure 4.9 Interfacial contact resistance (ICR) of bare AISI 304 and copper plate.

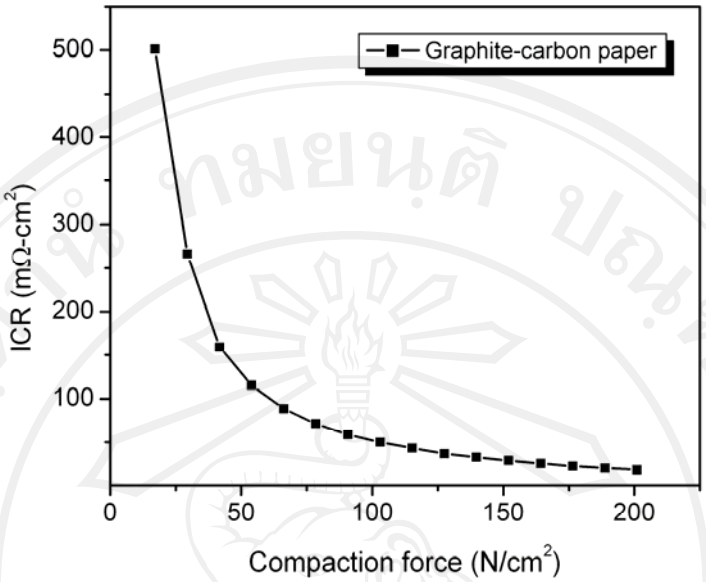

Figure 4.10 Interfacial contact resistance (ICR) of ET10 graphite and carbon paper.

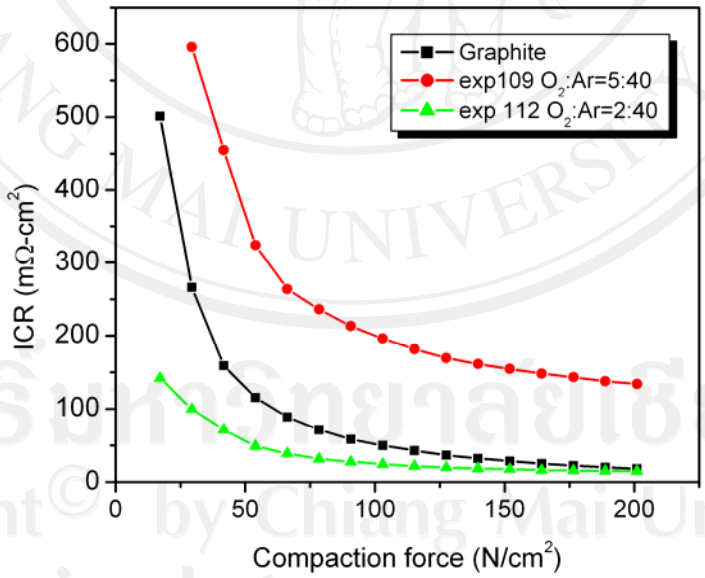

Figure 4.11 Interfacial contact resistance (ICR) of AISI 304 coated with ZnO:Al film and carbon paper.

The ICR of experiments exp110 and exp111 too high compare to exp109 and exp112. Figure 4.11 was not show the ICR of exp110 and exp111.

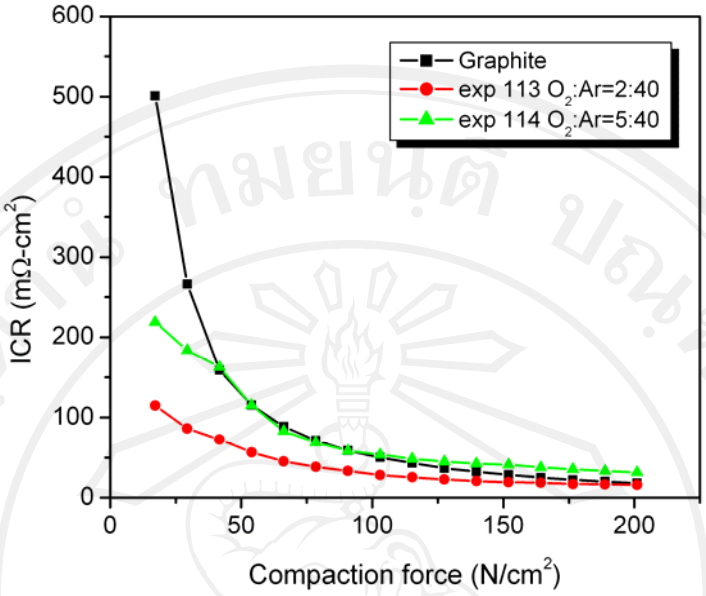

Figure 4.12 Interfacial contact resistance (ICR) of AISI 304 coated with ZnO film and carbon paper.

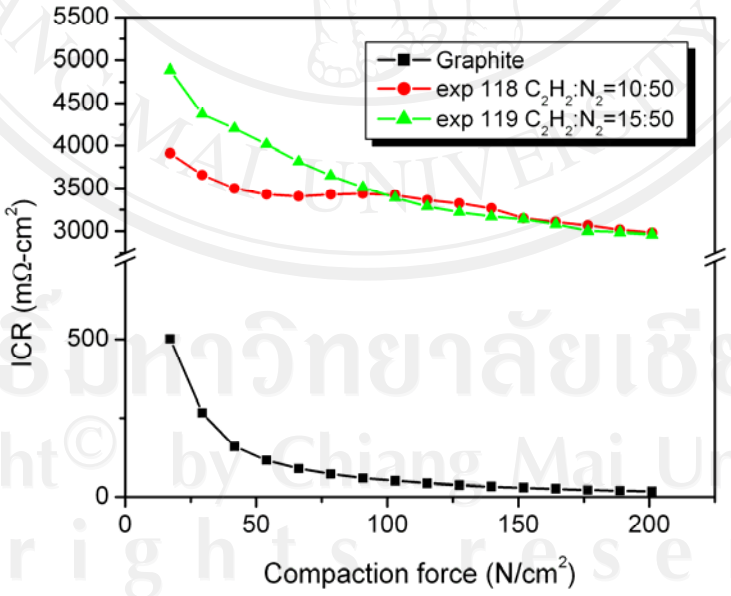

Figure 4.13 Interfacial contact resistance (ICR) of C_2H_4 and N_2 plasma treated AISI 304 and carbon paper.

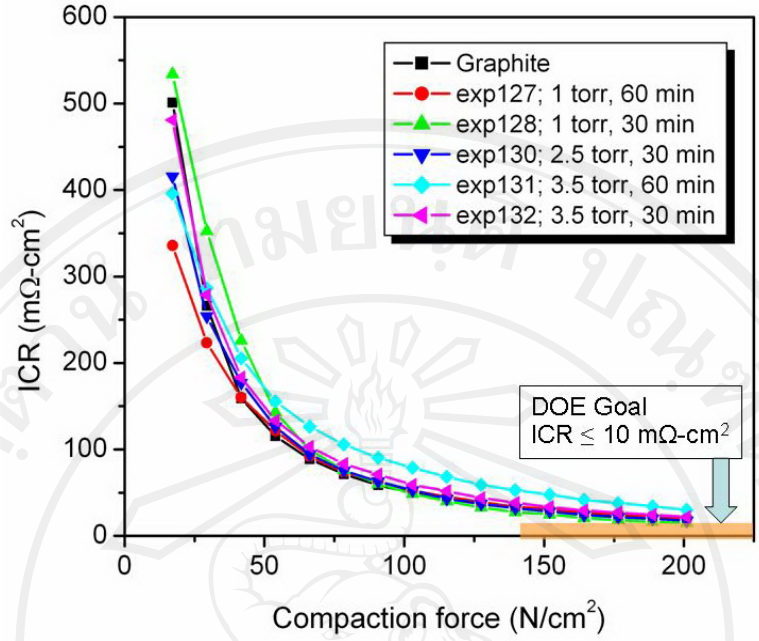

Figure 4.14 Interfacial contact resistance (ICR) of AISI 304 plasma nitrided by Pinnacle plus power supply and carbon paper.

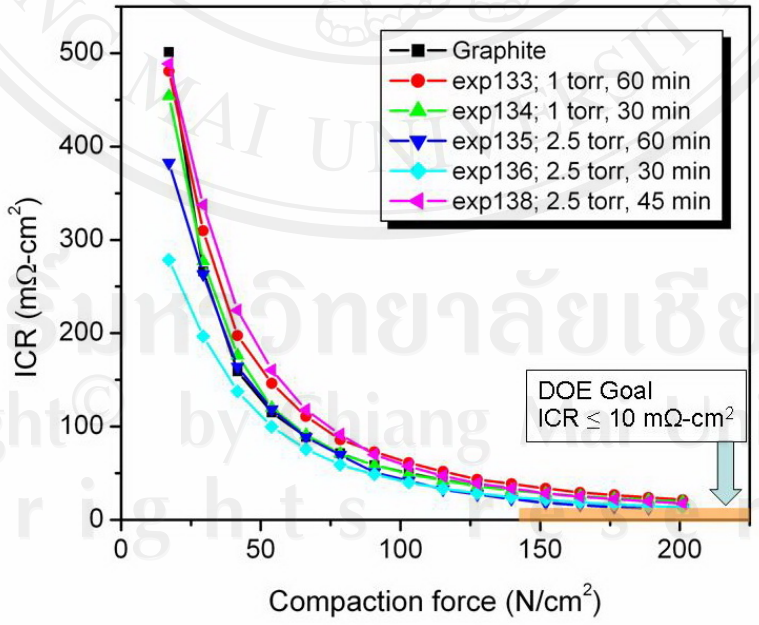

Figure 4.15 Interfacial contact resistance (ICR) of AISI 304 plasma nitrided by Cober power supply and carbon paper.

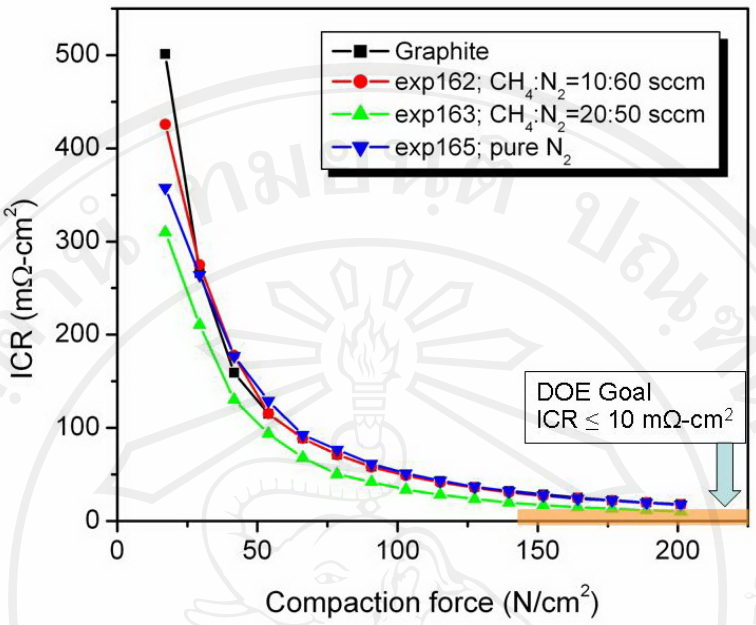

Figure 4.16 Interfacial contact resistance (ICR) of CH_4 and N_2 plasma treated AISI 304 and carbon paper.

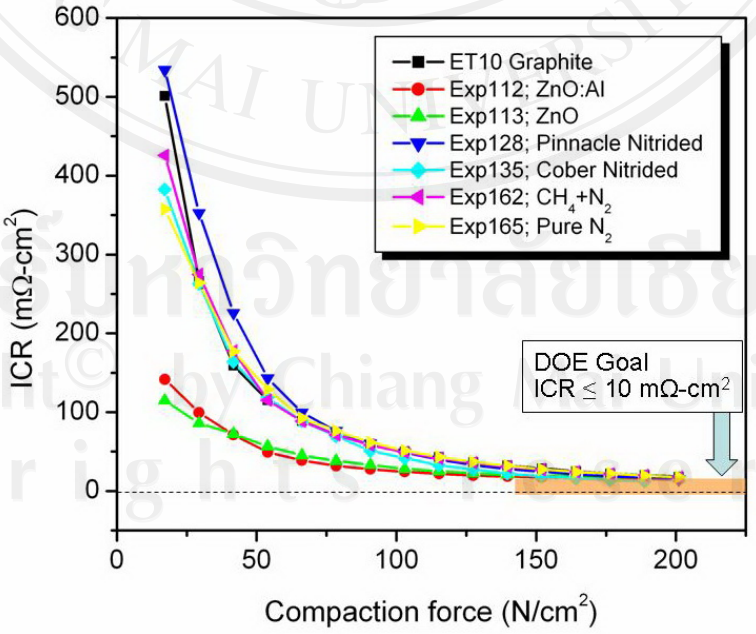

Figure 4.17 The best ICR of the specimens relevant to ET10 graphite.

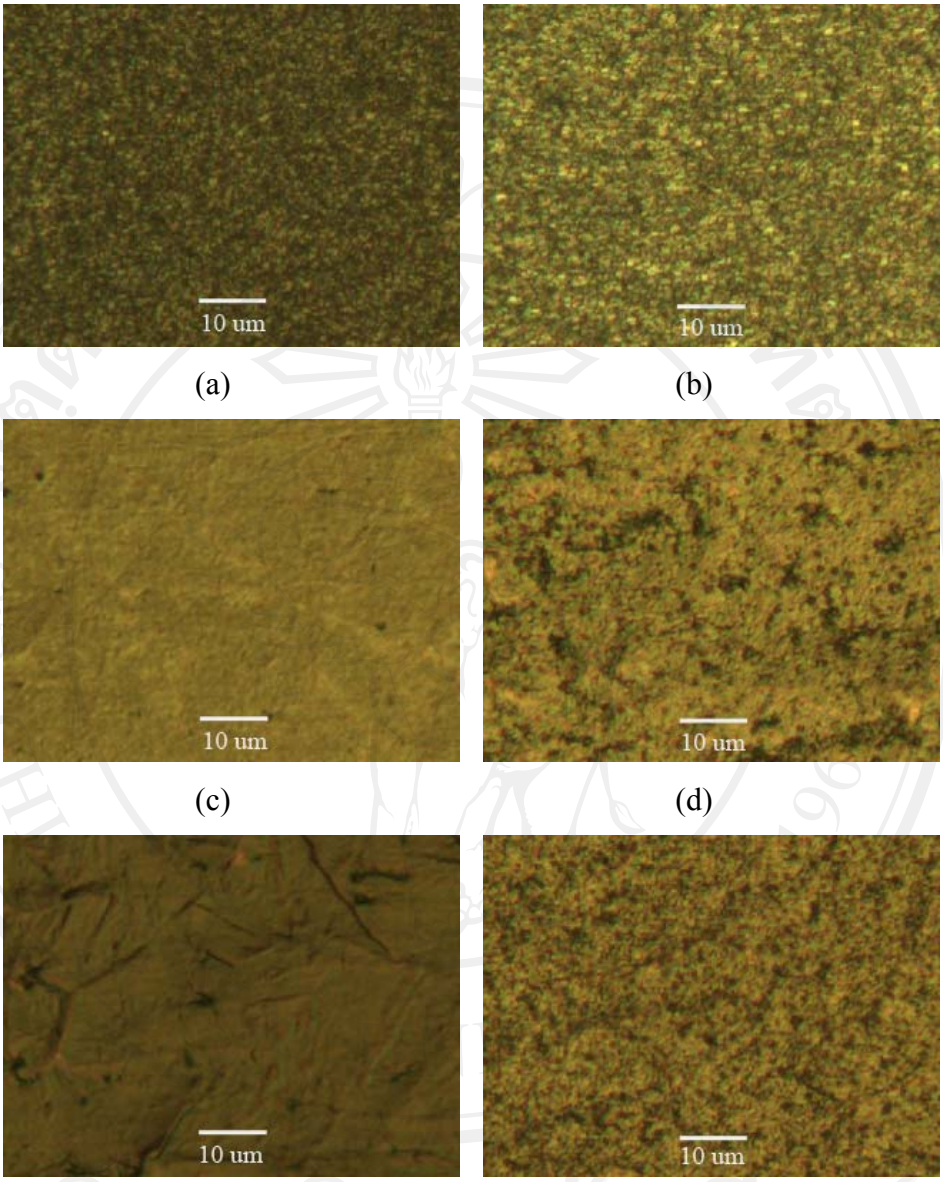

Figure 4.18 Optical microscopic picture of the most best treated ICR specimens.

(a). ZnO:Al film coated

(b) ZnO film coated

(c) Plasma nitriding by pinnacle plus power supply

(d) Plasma nitriding by cober power supply

(e) CH_4 and N_2 plasma treatemt

(f) Pure N_2 plasma nitriding

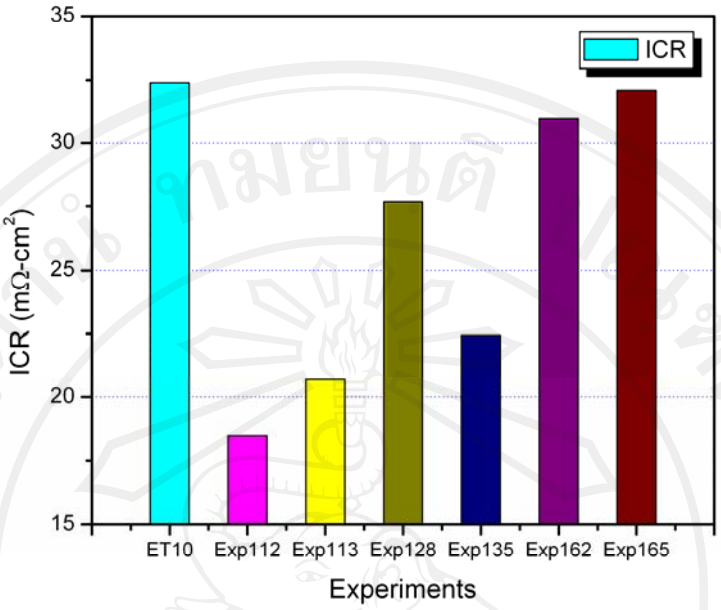

Figure 4.19 ICR (bars) at the compaction force of 140 N/cm^2.

DOE 2010 Goal; ICR ≤ 10 mΩ cm^2 at the compaction force ≥ 140 N cm^{-2}.

4.2.2 Atomic concentration depth profile

To confirm the formation of the nitride or carbide surface on the treated surface, the atomic depth profile of treated surface were analyse by glow discharge optical emission spectroscopy (GDOES). This analysis assisted by our co-researcher at Institutto de Ciencia de Materiales de Madrid, Spain. GDOES depth profile analysis of the coatings was completed using a Jobin Yvon RF GD Profiler equipped with a 4 mm diameter anode and operating at a typical radio frequency discharge pressure of 650 Pa and power of 40 W. The chamber was cleaned by sputtering a silicon (100) sample for 20 minutes, thereby covering potential sources of contamination. Before every experiment, the samples were flushed with argon for 60 seconds. A collection rate of 200 points/second was used to measure each sample. The setup was calibrated using standard materials of known composition. In order to improve the nitrogen calibration, chromium nitride coatings deposited by magnetron sputtering were used as reference materials (Galindo et al., 2007). The results shown as follow.

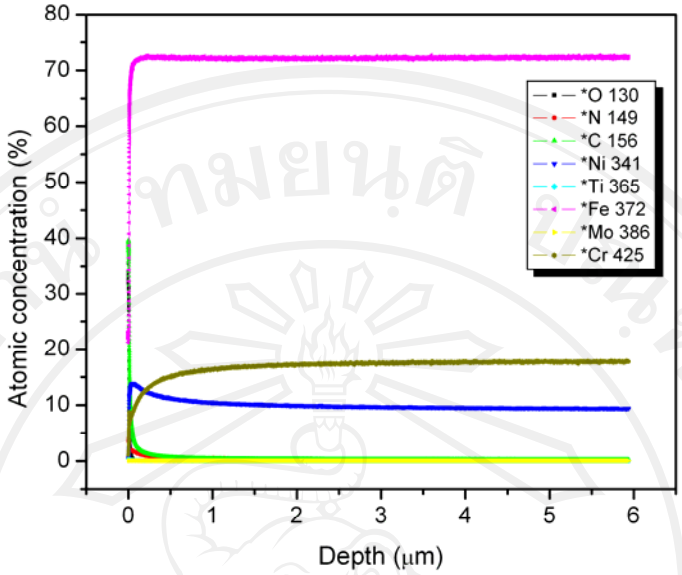

Figure 4.20 Depth profile of bare AISI 304 analyze by Glow Discharge Optical Emission Spectroscopy (GDOES).

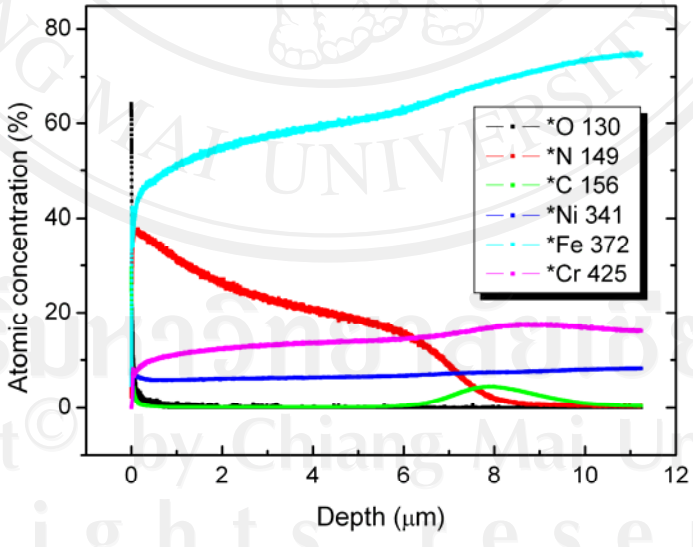

Figure 4.21 Depth profile of AISI 304 plasma nitrided exp 225 (the same condition as exp135).

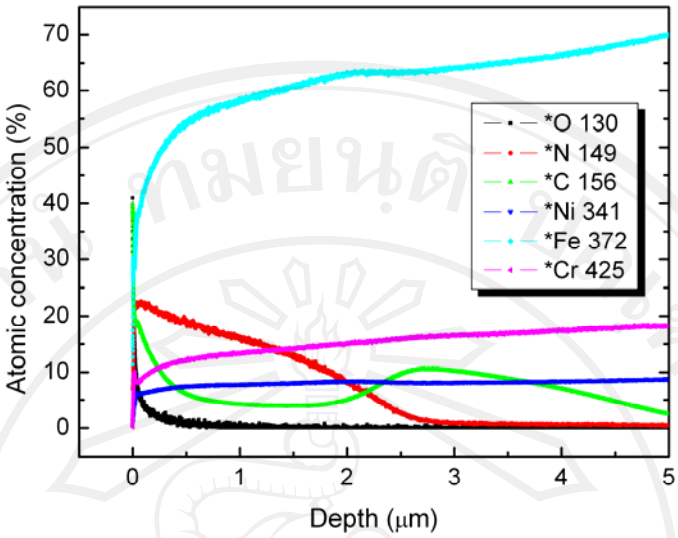

Figure 4.22 Depth profile of AISI 304 plasma nitrided exp 224 (the same condition as exp 162).

4.2.3 Static water contact angle

The static water contact angle was measured between the surface of a drop of water and treated surface. The experiment performed in room temperature (25˚C). The contact angle of different surface was shown in Figure 4.23.

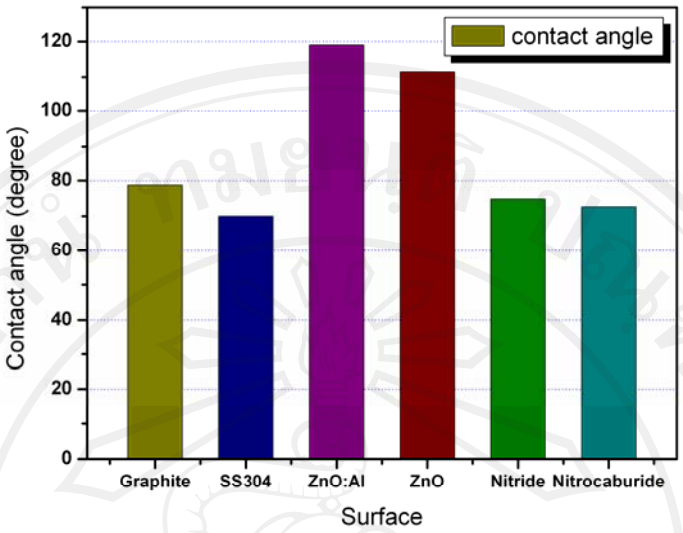

Figure 4.23 Static water contact angle of different treated surface.

4.2.4 Potentiodynamics polarization curve

Corrosion test following ASTM G5 standard (ASTM G5-94), with 1 M H_2SO_4 solution at room temp. Exposed area was 0.785 cm^2. Corrosion rate were obtained by SoftCorr III software. The potentiodynamics polarization curve and corrosion rate are shown in Figure 4.24 and Table 4.9, respectively.

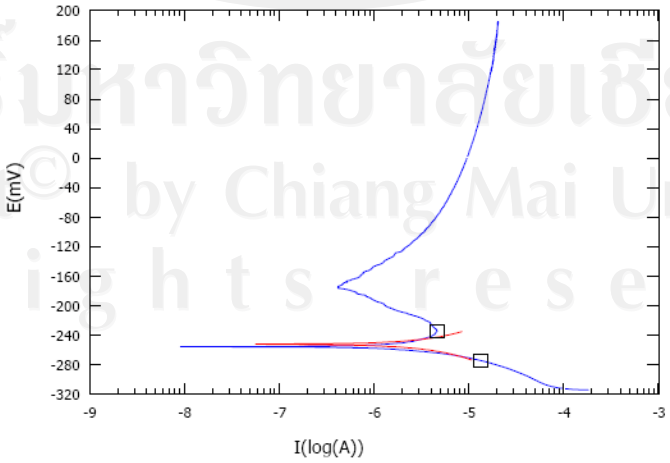

a). Polarization curve of Bare AISI 304.

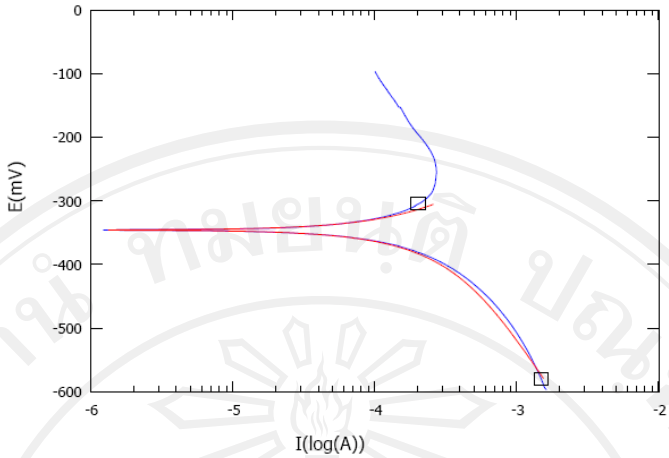

b). Polarization curve of ZnO coated AISI 304 surface.

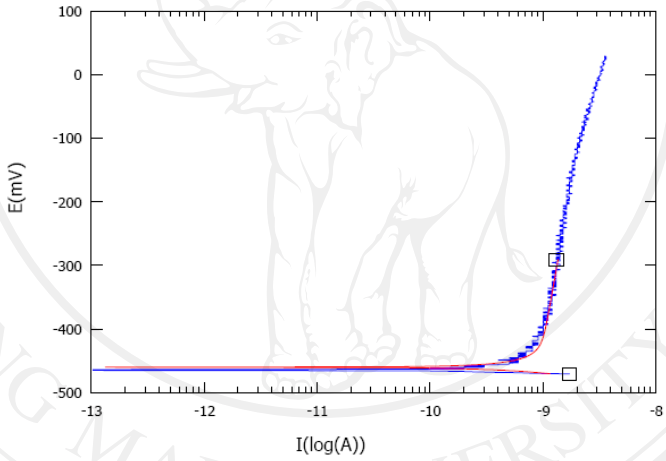

c). Polarization curve of ZnO:Al coated AISI 304 surface.

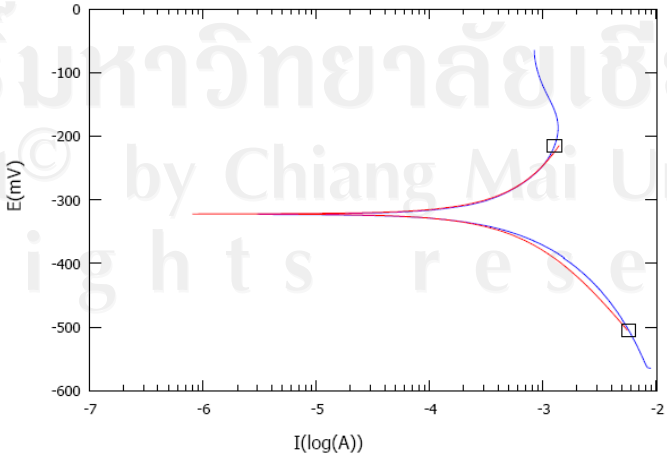

d). Polarization curve of nitrided AISI 304.

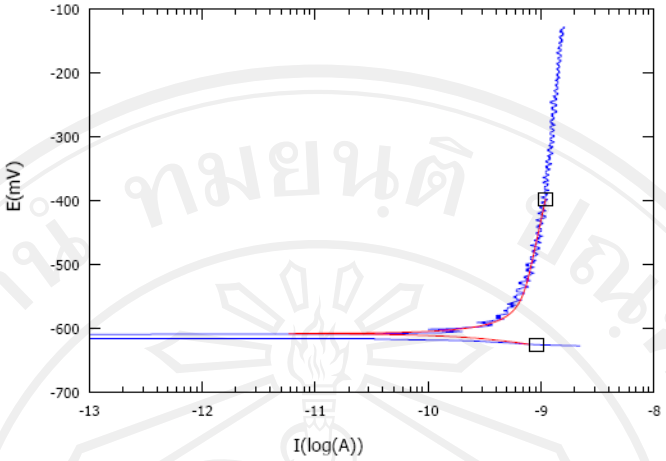

e). Polarization curve of nitride carburized AISI 304.

Figure 4.24 Polarization curve of the coated surface.

Table 4.9 Corrosion current and corrosion rate.

Coating	I_{corr}	Corrosion rate (mpy)[a]
Bare SS304	10.28 µA	5.355
ZnO (exp 229 as exp 113)	320.9 µA	167.1
ZnO:Al (exp 232 as exp 112)	910.7 pA	474.3E-6
Nitride (exp 225 as exp135)	952.0 µA	495.8
Nitride +Carbide(exp224 as exp 162)	606.1 pA	315.7E-6

[a] mill-inch per year = 2.54×10^{-5} meter per year

4.2.5 Coated AISI 304 fuel cell bipolar plates

The best conditions (lowest ICR) of each coating were applied to AISI 304 stainless steel bipolar plats. The selected condition are exp112 for ZnO:Al, exp113 for ZnO, exp135 for N_2+4%H_2 plasma nitriding and exp162 for N_2+CH_4 plasma nitrocarburizing. The results show as follow.

Figure 4.25 Photo of ZnO:Al coating bipolar plate (a) and ZnO coating bipolar plate (b) by reactive magnetron sputtering.

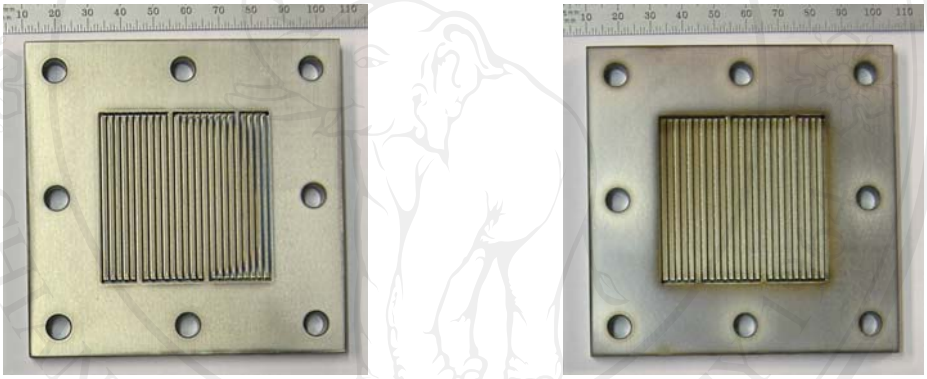

Figure 4.26 Photo of plasma nitriding bipolar plate (a) and plasma nitrocarburizing bipolar plate (b).

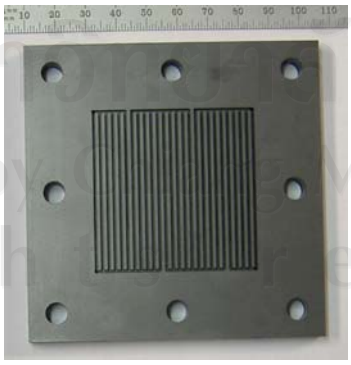

Figure 4.27 Photo of ET10 graphite bipolar plate.

During the plasma immersion process, the temperature of the bipolar plate was detected by an infrared thermocouple sensor. The temperatures were shown in Figure 4.28.

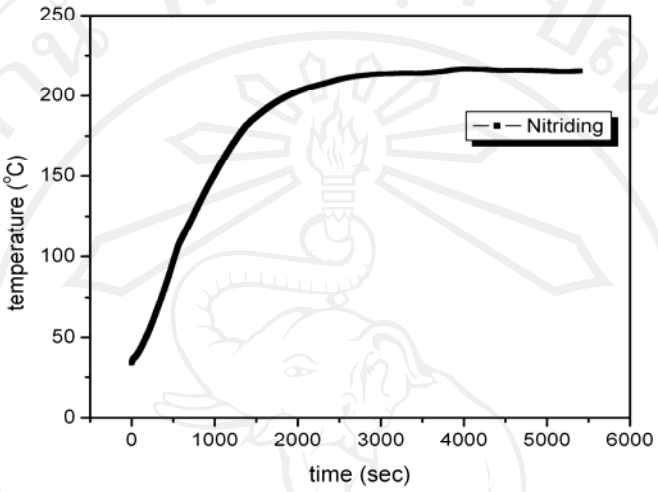

(a)

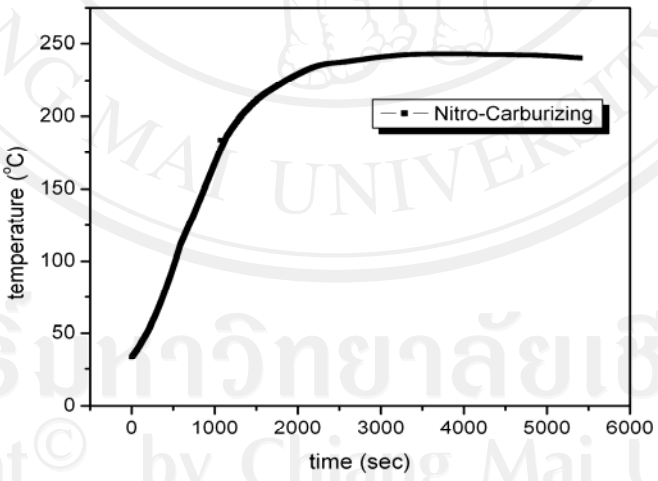

(b)

Figure 4.28 Temperature during bipolar plate treatment of plasma nitriding (a) and plasma nitrocarburizing (b).

4.2.6 Fuel cell polarization curve

To evaluate the performance of the metallic bipolar plates, single cells were fabricated using ET10 graphite, bare AISI 304, nitrided AISI 304, and nitride carburized AISI 304 stainless steel bipolar plates. The next two figure shows the initial performance of the single cells operated at a temperature of 65˚C, operating at a pressure of 1 bar, and the stoichiometry of fuel and oxidant was λ_{H2}=1.5 and λ_{O2}=2.0, respectively. Before the measurements, the single cells were operated for 20 hour for activation.

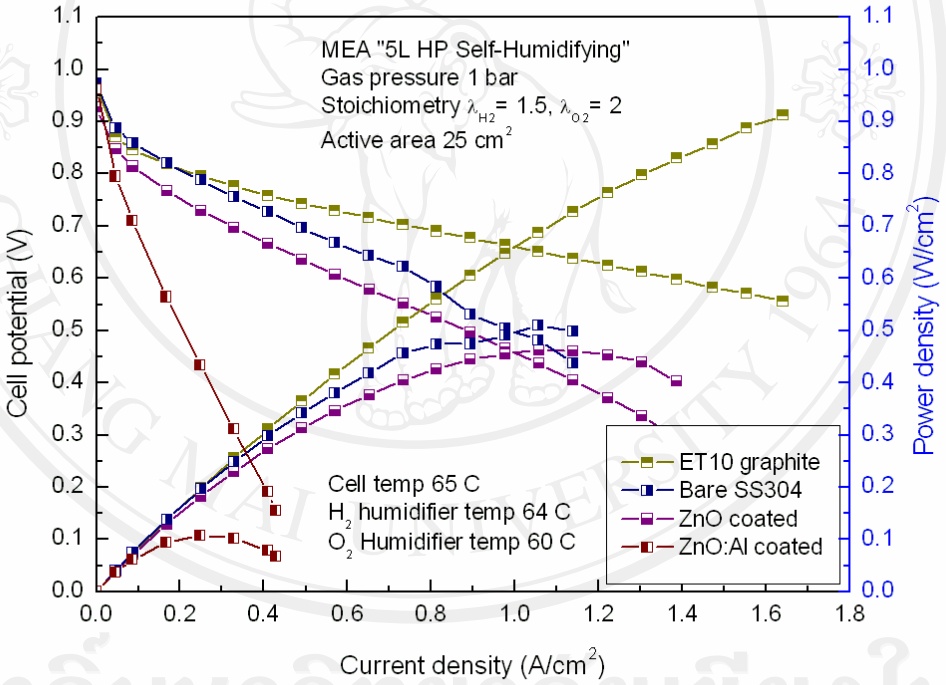

Figure 4.29 Current-voltage and current-power density performance of PEMFC with ZnO and ZnO:Al coated AISI 304 bipolar plates comparison with ET-10 graphite and bare AISI 304 bipolar plates.

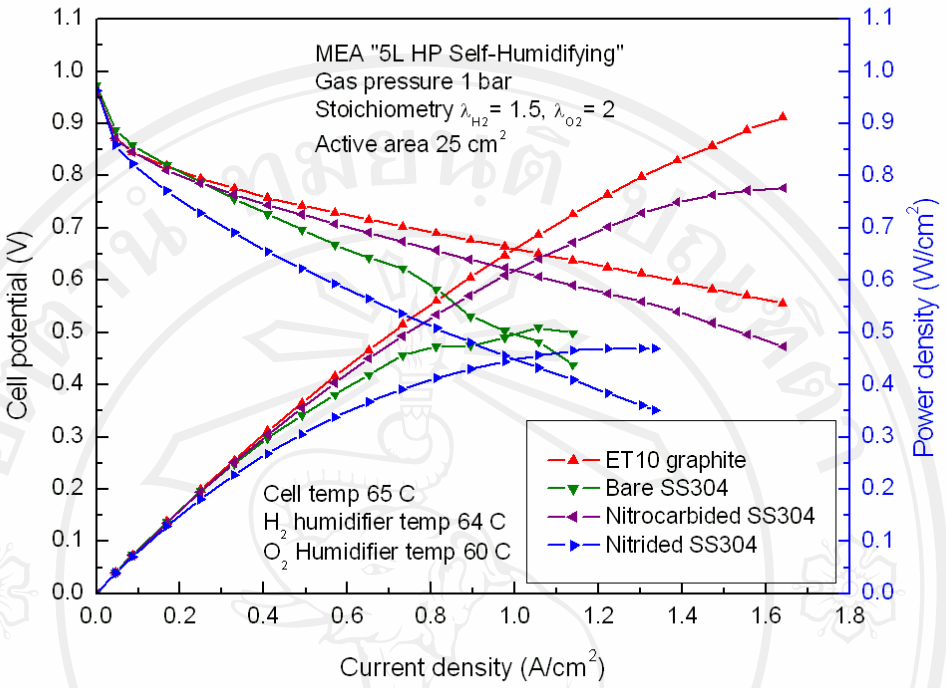

Figure 4.30 Current-voltage and current-power density performance of PEMFC with treated AISI 304 bipolar plates comparison with ET-10 graphite and bare AISI 304 bipolar plates.

As discussed in chapter 2, the fuel cell polarization curve has three distinct regions. The center region at intermediate current density is voltage losses due to ohmic losses (cell resistance). The cell potential drops linearly with current. Thus, a linear approximation is actually a very good fit for fuel cell resistance. Linear polarization curve has the following form:

$$V_{cell} = V_0 - k \cdot i \quad , \tag{4.1}$$

where V_0 is the intercept, and k is the slope of the curve which indicated cell resistance.

By linear curve fitting (shown in appendix B-3), we had the fuel cell resistance shown in Table 4.10.

Table 4.10 Fuel cell resistance with coated bipolar plates (BP).

Fuel cell with coating BP	Cell resistance (Ω cm^2)
ET 10 graphite BP	0.17
Bare AISI 304 BP	0.39
ZnO coating BP	0.37
ZnO:Al coating BP	1.60
Nitride BP	0.34
Nitride Carburized BP	0.22

In conclusion, the metallic bipolar plates exhibited lower performance than graphite, probably due to the higher contact resistance increasing after modified. The high surface energy of bare AISI 304 stainless steel could additionally reduce the cell performance particularly at high current densities as shown in Figure 4.29 and 4.30. In addition, corrosion of the metallic bipolar plates during the activation process could reduce the cell performance. However, the results show that at the cell voltage of 0.6 V, the single cells employing graphite still show highest power density.